

Article

Effect of Abnormal Grains on the Mechanical Properties of FGH96 Solid-State Diffusion Bonding Joint

Jingqing Zhang ¹, Yong Shang ^{2,*}, Qiaomu Liu ^{2,*}, Junwu Wang ³, Yanling Pei ², Shusuo Li ³ and Shengkai Gong ²

¹ School of Materials Science and Engineering, Beihang University, Beijing 100191, China; zhangjingqing0320@126.com

² Research Institute for Frontier Science, Beihang University, Beijing 100191, China; peiyanling@buaa.edu.cn (Y.P.); gongsk@buaa.edu.cn (S.G.)

³ Institute of Aero Engine Research, Beihang University, No. 37 Xueyuan Road, Beijing 100191, China; wangjunwu916@163.com (J.W.); lishs@buaa.edu.cn (S.L.)

* Correspondence: cs881013@buaa.edu.cn (Y.S.); lqiaomu@163.com (Q.L.)

Abstract: The hollow twin-web disk is designed to improve the thrust-to-weight ratio of the aero engine, where the welding joint microstructures determine the disk's mechanical properties. This study aimed to elucidate the effect of abnormal grains formed in the welding region on the mechanical properties of FGH96 solid-state diffusion bonding joints. Digital image correlation using images captured by scanning electron microscopy (SEM-DIC) and electron backscattering diffraction (EBSD) technologies were applied. The results show that abnormally large grains (2.5 times that of the matrix), with preferred orientation in the bonding region, were detrimental to the joint mechanical properties. The yield and tensile strengths were 995.85 MPa and 1456.67 MPa, respectively, and the corresponding relative (ratio to the matrix) ones were 92.54% and 88.81%. After modifying the bonding process, the grain size in the bonding region was tailored to close to that of the matrix, and considerable twin boundaries (TBs) formed, leading to the relative tensile and yield strength reaching 98.86% and 99.37%. Furthermore, the failure mode changed to intragranular type from intergranular type. It demonstrates that tailoring the newborn grain size, introducing TBs inside, and eliminating preferred orientation during the welding process can be an efficient way to improve the joint mechanical properties.

Keywords: FGH96 joint; welding; abnormal grain; grain orientation; twin boundary; failure



Citation: Zhang, J.; Shang, Y.; Liu, Q.; Wang, J.; Pei, Y.; Li, S.; Gong, S. Effect of Abnormal Grains on the Mechanical Properties of FGH96 Solid-State Diffusion Bonding Joint. *Crystals* **2022**, *12*, 1017. <https://doi.org/10.3390/cryst12081017>

Academic Editors: Hongbin Bei and Pavel Lukáč

Received: 23 June 2022

Accepted: 20 July 2022

Published: 22 July 2022

Publisher's Note: MDPI stays neutral with regard to jurisdictional claims in published maps and institutional affiliations.



Copyright: © 2022 by the authors. Licensee MDPI, Basel, Switzerland. This article is an open access article distributed under the terms and conditions of the Creative Commons Attribution (CC BY) license (<https://creativecommons.org/licenses/by/4.0/>).

1. Introduction

The powder metallurgy (PM) Ni-based superalloys exhibit many excellent performances compared to the conventional wrought superalloys, such as the uniformity of composition, high damage tolerance, and oxidation resistance [1,2]. As a typical 2nd-generation PM Ni-based superalloy, FGH96 is widely used to manufacture turbine disks [3,4]. In order to improve the thrust-to-weight ratio, the traditional single-web turbine disk was supposed to be substituted by hollow twin-web turbine disks (TWD), which are conducive to weight reduction and cooling efficiency [5–7]. The welding techniques were applied to produce the hollow profiles, among which the solid-state diffusion bonding (SSDB) process was considered a prevailing method, since it can avoid the formation of adverse phases in the bonding regions, such as blocky brittle phases or intermetallic compounds, which are inescapable during the transient liquid phase bonding and braze welding [8–10]. Due to the microstructure discrepancy between the welding areas and the matrix regions, the welding region was usually the weak zone of the joint and determined the mechanical properties of the TWD. Therefore, it is important to study the microstructures formed in different welding processes and their effects on the mechanical properties of bonding joints.

The microstructure features in the welding zone, such as the grain sizes, orientation distribution, and the grain boundary characterization distribution (GBCD), were decided

by the welding processes, for example, the bonding temperature and pressures, the initial material states, and the pure Ni interlayer application [11–13]. All the above microstructure features can strongly influence the material properties, including the physical and chemical properties [14–17], and mechanical properties [18–22], which are widely studied in different based materials (BMs). However, few studies were accessible for the SSDB joints.

It is well known that grain sizes influence mechanical properties and failure mode. For example, the yield strength, tensile strength, and fracture elongation decreased with increasing the grain size in nickel-based superalloy deformed at room temperature [23]. While in the studies of Maowen Liu and F.K. Yan [24,25], excellent strength ductility synergy was accomplished in the recrystallized 316 stainless steel by tailoring grain size into the nanoscale. Similar studies were carried out on magnesium [26], and a simultaneous increase in strength and ductility were achieved by tailoring the grain size from 125 μm to 51 and 5.5 μm , due to the activation of non-basal slip systems and the formation of nano-spaced stacking faults, where the activation of more dislocations helped to accommodate strain and improve the uniform elongation, and the high density of nano-spaced stacking faults acted as an additional strengthening mechanism. The grain size also influenced the failure mode. Tim P. Gabb [27,28] revealed that the specimens with a fine grain failed mostly from internal inclusions, while those with coarse grains always failed from crystallographic facets.

In addition to the grain size, the grain orientations also have an impact on the mechanical properties, which are significantly outstanding in the single crystal superalloys, excluding the effect of high-angle grain boundaries (HAGB) and twin boundaries (TBs) [29–32]. Yifei Li [29] found that the [111] orientated specimens displayed the longest creep life at 850 °C for a 3rd generation single crystal superalloy, the [11] one showed the shortest creep life and longest elongation, and the [1] one presented the intermediate performance. This phenomenon was related to the different activated slip systems and their interactions at different stages for the specimens with different orientations. Other studies [33,34] also revealed that the activation of different slip systems (cube slip or octahedral slip systems) was mainly affected by the crystal orientation at intermediate or low temperatures, and then affected the fatigue properties. Shiqi Zhang [35] figured out that the geometric necessary dislocations (GNDs) density had a strong orientation dependency during the monotonic deformation of aluminum alloy: $\langle 111 \rangle$ orientated grains with a higher Taylor factor accumulated more GNDs than $\langle 100 \rangle$ orientated grains, which was attributed to the fact that higher Taylor factor grains required larger stress to realize uniform geometrical change.

Moreover, TBs play a vital role in adjusting the mechanical properties. Numerous studies [36–38] demonstrated that twinning could produce a much improved strength without sacrificing resistance to fracture due to the coherent nature of TBs. Depending on its characterization, this kind of boundary can block or transmit the slip and thus provide strength and ductility [37]. Shiteng Zhao [38] showed a bulk nanostructuring method to make a pure Ti achieve an ultimate tensile strength of almost 2 GPa and a true failure strain close to 100% at 77 K by introducing a multiscale, hierarchical twin architecture into the coarse-grained titanium, which diminished the trade-off between the strength and ductility. The pre-twinning strategy, based on stacking fault energy (SFE) controlling in medium Mn steel, provided continuous hardening capacity after yield; consequently, the tensile strength increased by 1.7 times with an acceptable ductility via alleviating shear strain accumulation and retarding crack initiation [39].

Up to now, many studies [21,38,40,41] have indicated an inner relationship among grain size, grain orientation, and TBs numbers, which comprehensively affect the material properties. Bingshu Wang [40] reported that although higher yield strength was produced in the small grains, deformation twinning was favored in larger grains and affected by the grain orientation. Finally, twin–twin interactions in large grains also promote hardening. It is also proposed that too large or too small grains are not conducive to the TBs formation [38]. M. Sarkari Khorrani [42] showed that the formation of abnormally grown grains is concomitant with the development of {001} $\langle 100 \rangle$ cube and {110} $\langle 001 \rangle$ Goss texture components in deformed aluminum alloy. Furthermore, the pre-existing preferred

orientation in the deformed alloy can, in turn, enhance the incubation of abnormal grain growth [43]. R.T. Ott [41] studied the dependence of the strength and ductility on the twin density and orientations of ultra-fine grained Ag, which presented that the untwinned grains provided decreased strength compared with twinned grains due to relatively low resistance to slip, and the twinned grains without $\langle 111 \rangle$ orientation were softer than those with $\langle 111 \rangle$ orientation.

The formers' studies suggest that the microstructures correlated with grain size, orientation, and TBs can offer crucial information for the strengthening and toughening mechanism, and provide consults for reinforcement in metal alloys. Therefore, it can be deduced that these factors and mechanisms may also be suitable for PM superalloy SSDB joints. However, up to now, the accessible information on the research was still poor, and no detailed analysis was carried out on the PM superalloy SSDB joints.

In the present study, the relationship among the three factors (grain size, orientation, and TBs) and their effects on the mechanical properties of FGH96 SSDB joints were studied, and then the microscopic mechanism was analyzed, which could lend sight into tailor grain microstructures and improve the mechanical properties of the SSDB joint.

2. Materials and Methods

2.1. Materials

The chemical composition of the BMs (a PM superalloy FGH96) is summarized in Table 1. PM FGH96 alloy cylinders with a diameter of 40 mm and a height of 40 mm were welded through the SSDB technique using a 5–10 μm pure Ni interlayer by electroplating. The cylinders were bonded at 1140 °C under 8–10 MPa for 1 h in a vacuum less than 7×10^{-3} Pa and cooled in the furnace. The bonding temperature and time were chosen according to the solution treatment of FGH96 carried out at 1127 °C~1150 °C for 2 h. Two bonding processes were designed, as shown in Figure 1, which were carried out by the Beijing Institute of Aeronautical Materials. For the first process, the initial condition of the FGH96 for bonding was a supersolvus solid solution state. After the bonding process, the joint was aged at 760 °C for 16 h to adjust the morphology of γ' , which was named the original bonding process. The other bonding process was named the modified bonding process, where the initial condition of the FGH96 for bonding was a hot forging state (with a total 60% deformation and a 0.1 mm/s reduction rate at 1050 °C), then the joint was treated through the standard supersolvus solid solution heat treatment (1150 °C for 2 h) and aging heat treatment (760 °C for 16 h).

Table 1. Chemical composition of base material (BM), i.e., FGH 96 superalloy, in this study.

Composition (wt.%)										
Co	Cr	Mo	W	Al	Ti	Nb	Zr	C	B	Ni
12.5~13.5	15.5~16.5	3.8~4.2	3.8~4.2	2.0~2.4	3.5~3.9	0.6~1.0	0.025~0.05	0.02~0.05	0.006~0.015	Bal.

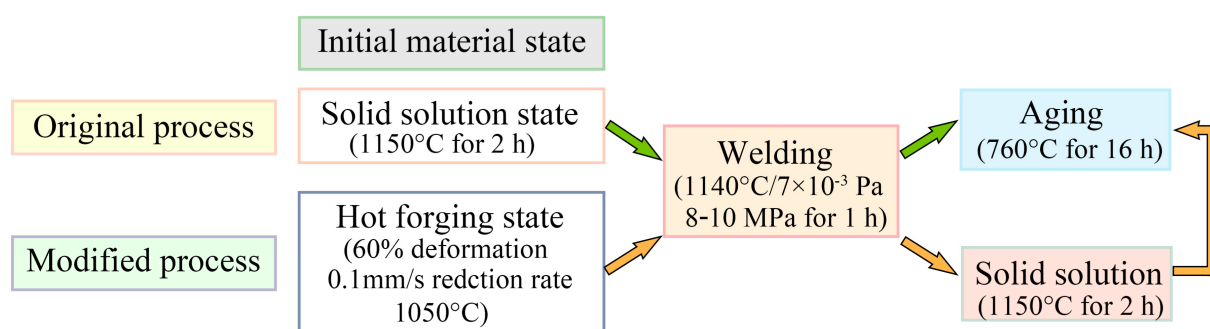


Figure 1. The flowchart for welding processes with two different initial material states.

2.2. Methods and Characterization

Dog-bone-shaped, sheet-type tensile specimens with a gauge length of 25 mm, gauge width of 3 mm, thickness of 1 mm, and with the bonding region sited in the middle of the gage length, were cut from the bonded cylinders, which were used for the uniaxial tensile test at room temperature with a strain rate of $4.2 \times 10^{-4} \text{ s}^{-1}$. As a comparison, the BMs that followed the same welding thermal cycle were also made into tensile specimens with the same dimensions. The quasi in situ tensile experiments [44] were performed and the specimens were tensile-deformed to different strains of 4%, 9%, and 15%. The microscopic strain distributions in the bonding region and neighboring matrix zone were analyzed by the digital image correlation (DIC) technique using secondary electron (SE) images captured by scanning electron microscopy (SEM), i.e., the SEM-DIC technique. The Vic-2D software (version 2009.1.0, Correlated Solutions Inc., Columbia, DC, USA) was applied as the postprocessing tool for the strain calculation. Secondary γ' with a size of 100–200 nm in FGH 96 was chosen as a speckle pattern to achieve a strain field at a sub-micron resolution. Furthermore, the evolutions of crystallography messages during the quasi in situ tensile experiments were analyzed by the electron backscattering diffraction (EBSD) technique. All the microstructure characterizations were conducted by SEM (Apreo S LoVac, FEI, Czech) equipped with an EBSD system operated at 25 kV. In order to track the microstructure evolution of the joint, tensile testing was interrupted for EBSD scans and taking images for DIC on the same area of interest (AOI) between successive steps. The detailed operations can be referred to the article [44]. The dislocation morphologies in deformed samples were identified by a transmission electron microscope (TEM, JEM2100, Tokyo, Japan) operated at 200 kV.

3. Results

3.1. Microstructural Characterization of FGH96 SSDB Joints

Figure 2 showed the microstructures of the FGH96 SSDB joints with different bonding processes. The EBSD orientation image microscopy (OIM) maps, where colors indicate the crystallographic orientation parallel to the normal direction of the bonding interface, revealed that most newborn grains in the bonding region of the joint bonded by the original process (named the original joint in the following text) were rendered by violet color, suggesting the grains were with a preferential crystallographic texture, as shown in Figure 2a,b. Notably, these messages were sampled from at least three different specimens in different areas, making the observation statistically sound. In contrast, various colors were randomly distributed in different grains in the bonding region of the joint bonded by the modified bonding process (named the modified joint), and the grains of the BM followed the same welding thermal cycle (named the BM), which indicated no preferential crystallographic texture, as shown in Figure 2c,d. Furthermore, the standard stereographic orientation triangles (Figure 2e–h) for the grains in the bonding regions and BM verified that the grain orientation in the X-direction (the external stress) was mainly located near $\langle 111 \rangle$ polar, with fewer at $\langle 001 \rangle$ corner, and little at $\langle 110 \rangle$ corner for the original joint, while it was spread all over the triangle for the modified one and the BM.

Regarding the joints bonded with different processes, the grain sizes and GBCD for the grains in the bonding regions are shown in Figure 2i,j, accompanied by the same messages for the BM. The size of the newborn grains in the bonding region of the original joint was the largest (60.12 μm), almost three times that of the BM (24.06 μm). While the modified joint displayed a smaller newborn grain size (28.44 μm), which was equivalent to that of the BM. Identifying from the GBCD in Figure 2j, little TBs (only 1.98%) were obtained in the bonding region of the original joint. When the modified process was operated, the TBs in the bonding regions increased to 50.82%, which was the same amount as that of the BM.

The morphologies of γ' in different areas, from the bonding regions to the matrix zone, were shown in Figure 3, which indicates that the size and shapes of γ' were different for different regions. This discrepancy can be used to identify the failure location for tensile specimens.

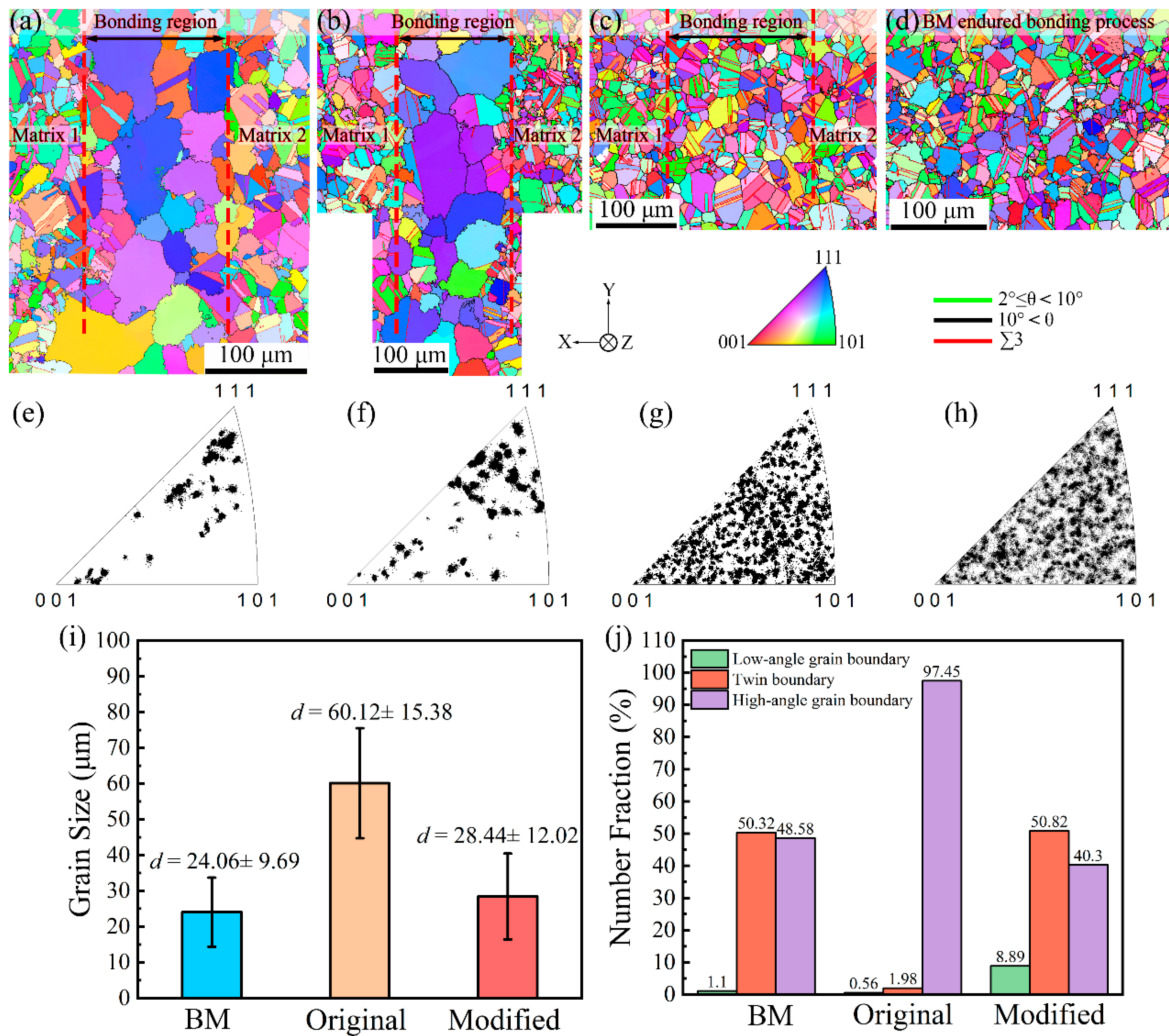


Figure 2. EBSD patterns of FG96 SSDB joints with different bonding processes and the BM endured the bonding thermal cycle. (a,b) Orientation image microscopy (OIM) maps in the X-direction (the normal direction of the bonding interface) of the joint bonded by the original bonding process. (c) The OIM map in the X-direction of the joint bonded by the modified bonding process. (d) The OIM map for the BM endured the welding thermal cycle. (e–h) The corresponding orientation distribution for the grains in the bonding region in (a–c), and the grains in the BM in (d). The grain size (i) and grain boundary character distribution (GBCD) (j) for the grains in the bonding region and BM.

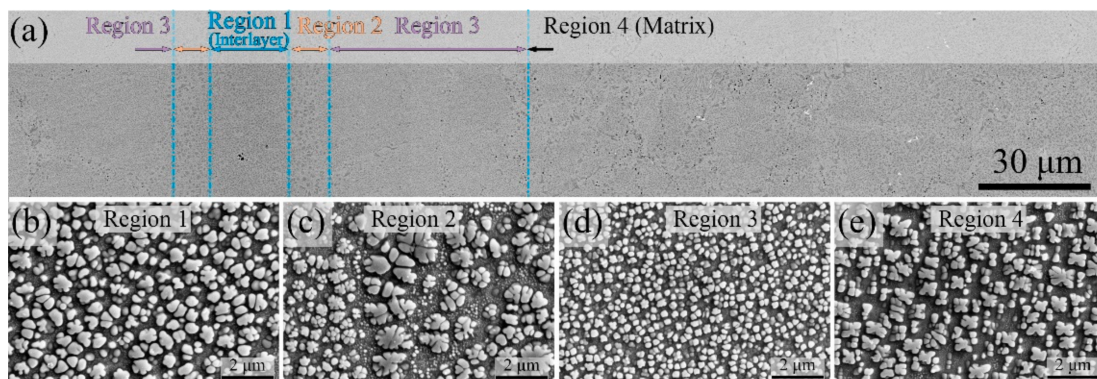


Figure 3. (a) Backscattered electron (BSE) images of FG96 SSDB joint from the bonding region to the matrix region, and the γ' morphology in different regions of (a): (b) region 1, (c) region 2, (d) region 3, and (e) region 4.

3.2. Mechanical Properties

Tensile strength, yield strength, and elongation of the different joints are displayed in Figure 4a, together with that of the BM. Furthermore, the relative strength and elongation, i.e., the ratio between the joint and the BM, are shown in Figure 4b. Moreover, the fracture morphologies of different samples are shown in Figure 4c–e. The tensile strength and yield strength of the original joint reached 1465.67 MPa and 995.85 MPa, which were 92.54% and 88.81% of that of the BM, respectively. Unexpectedly, the relative elongation reached 116.11%. When the bonding process was modified, the joint exhibited a tensile strength of 1583.86 MPa and yield strength of 1121.27 MPa, with a relative tensile strength of 98.86% and yield strength of 99.37%. Obviously, these values were improved largely, compared with the original joint. However, the relative elongation decreased to 95.25%.

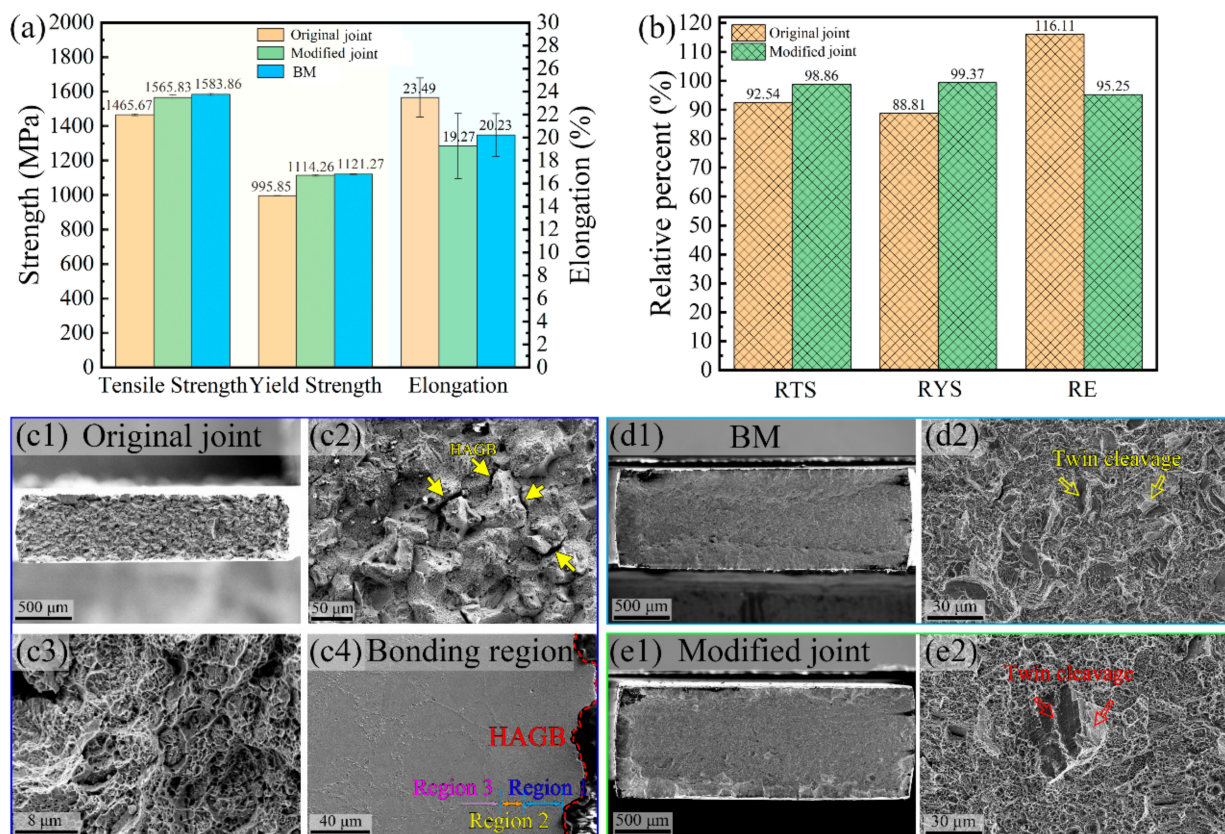


Figure 4. Tensile strength, yield strength, and elongation of the SSDB joints and BM endured with the same bonding process (a), and the relative strength and elongation for different joints (b). Fracture morphology of SSDB joint with different bonding processes (c1–c4,e1,e2) and BM (d1,d2).

The fracture morphologies (Figure 4c) showed that the fracture surfaces were rock candy-shaped and distributed with dimples, implying the typical ductile and intergranular fracture characteristics for the original joint. Identifying from the section profile (Figure 4(c4)), the fracture site of the joint was in the bonding region according to the joint microstructure (Figure 3). The relative position between the primary crack line and the high-angle grain boundaries (HAGB) displayed that the primary crack line coincided with the HAGB of the abnormally large grain, suggesting the crack propagated along the HAGB. However, the fracture morphologies of the modified joint and the BM were planar and distributed with dimples, implying the fracture type transferred into a ductile intragranular type. It is worth noting that some small planes arising from twin cleavage were distributed on the fracture surface, as shown in Figure 4(d2,e2), suggesting that the TBs played an important role in the deformation behavior.

4. Discussion

The results of this work show that abnormal large grains with preferred grain orientations and a small number of TBs formed in the bonding region of the FGH96 SSDB joint bonded by the original process, leading to relatively poor mechanical properties. After the bonding process was modified, the grain size in the bonding region was tailored to be similar to that of the BMs, accompanied by the same fraction of TBs, and the preferred grain orientation vanished. Then, the tensile mechanical properties were improved largely. Moreover, the fracture type transferred into the intergranular type from the intragranular type.

4.1. The Origin of Abnormal Grain Growth and Its Correlation with Preferred Grain Orientation and Twin Boundaries for the Newly Formed Grains in the Bonding Region

The grain growth during welding is not only related to the strain energy caused by the imposed external bonding stress but also to the material initial states before being bonded, such as the initial grain size, the secondary phases, and the reserved strain energy in the materials depending on the heat treatments. In order to qualitatively and quantitatively identify this information for the two different initial BMs used in this work, EBSD and SEM were applied. The obtained results are shown in Figure 5. It can be seen that many large primary γ' and smaller secondary ones precipitated at the grain boundaries or in the grain interior of the BM with a hot forging state, as shown in Figure 5c,d, while no γ' were found in the BM with a solid solution state, as presented in Figure 5a,b. Furthermore, the grain sizes were much different for the two BMs (See Figure 5i).

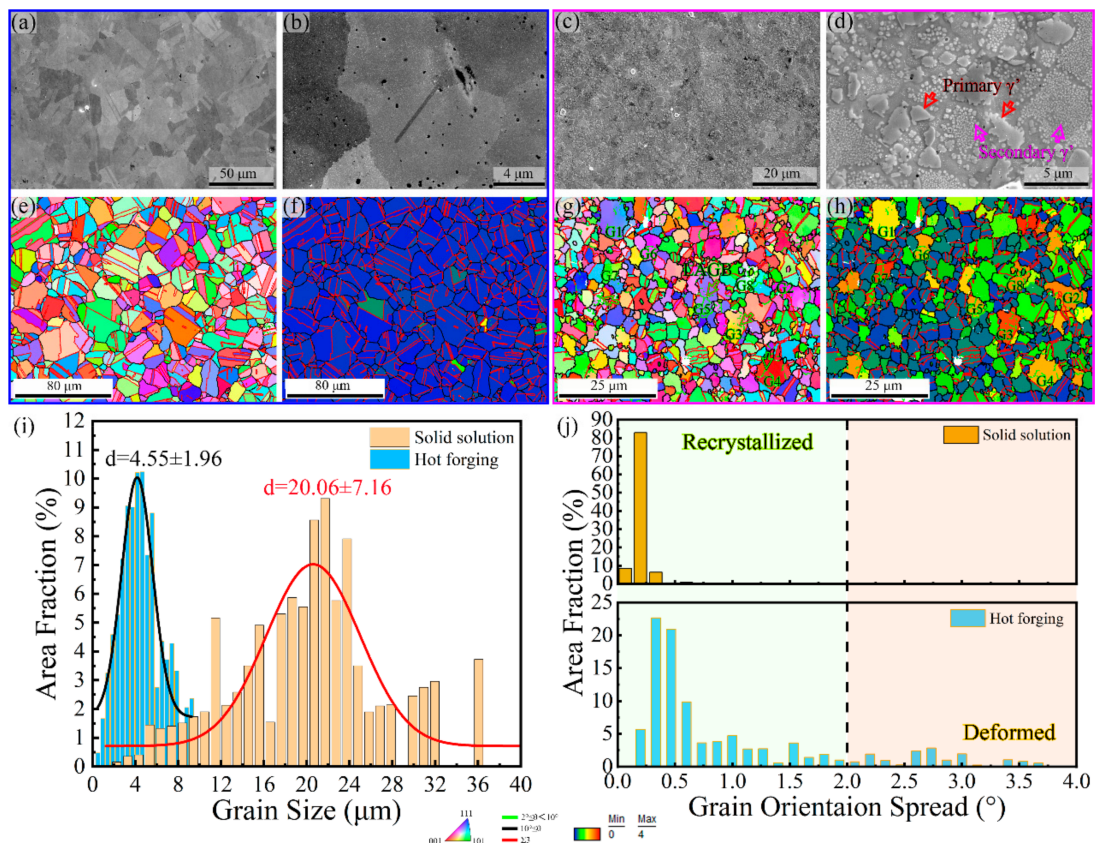


Figure 5. The microstructure characterization of the FGH96 base materials with different heat treatments. (a) Secondary electron (SE) images for solid solution (SS) treated state, and high magnification (b), (c) SE images for hot forging (HF) state, and high magnification (d). (e–h) are, respectively, the OIM map, grain orientation spread (GOS) map for SS state (e,f), and HF state (g,h). The grain size distribution (i) and the area fraction of grains with a specified GOS (j) for the two specimens are also statistically displayed.

The grain orientation spread (GOS) measures the orientation deviation between all the points within a grain relative to the average orientation for that grain and is commonly used to characterize recrystallization [45]. A critical of GOS $< 2^\circ$ for recrystallization is commonly used [45–48]. As a result, the GOS can be used as a credible index for identifying grain inhomogeneous deformation. In order to qualitatively identify the pre-existing strain in the initial materials before being bonded, the GOS was statistically analyzed, which is shown in Figure 5j. Furthermore, the visual GOS maps and the OIM maps are shown in Figure 5e–h for the two initial BMs with different heat treatments.

From the statistical results of GOS, it can be seen that all the GOS values for the grains in the BM with a solid solution state were less than 2° . Moreover, the orientation colors in the OIM map (Figure 5e) were homogeneously distributed, and no color gradients were presented within a single grain, suggesting that no deformed grains exist and the recrystallization is completed, i.e., negligible strain energy existed in the initial material. In contrast, grains with a GOS $> 2^\circ$ occupied a certain area fraction for the BM with a hot forging state. Furthermore, orientation gradients can be seen in many grains, such as the G1–G8 grains in Figure 5g, as inhomogeneous distributions of colors were within these grains in the OIM map. Moreover, these grains with inhomogeneous orientations presented larger GOS values and grain sizes, as revealed in Figure 5h, implying that the specimen was mostly, but not completely, recrystallized after the hot forging and some deformed grains were reserved [48], i.e., pre-existing nonnegligible strains reserved in the initial material. Furthermore, the remaining deformation and unfinished recrystallization can be reinforced by the tangled low-angle grain boundaries (LAGB) in the grains with larger GOS, as indexed by the arrows in Figure 5g. It can be supposed that all the differences in the initial microstructures of the BMs can lead to differences in the microstructure of the welding zone.

The BMs with a solid solution state were used as the initial materials when the original bonding process was carried out. As a result, the kinetics for the grain growth in the bonding process mainly come from the strain energy caused by the imposed bonding pressure, since negligible strain energy existed in the initial material due to the completed recrystallization. The imposed pressure (8–10 MPa for 1 h) brings out a larger strain in the pure Ni interlayer than that in the BMs due to solution strengthening; that is, more strain energy is stored in the pure Ni interlayer. In view of the fact that there was no prior strain energy in the BMs and a weak one was caused by the external stress in the bonding process, the grain growth mostly concentrates in the grains surrounding the pure Ni interlayer due to the strain-induced grain boundary migration [49], and this explains the result that the grain size (24 μm in Figure 2i) in the matrix region of the original joint is close to that (20 μm in Figure 5i) of the initial BM. The supersolvus heat temperature (1140 $^\circ\text{C}$) applied in the bonding process provides the thermodynamic condition for the grain growth. Driven by the thermodynamic and kinetic conditions, the grain boundaries on either side of the pure Ni interlayer would migrate, leading to the growth and coalescence of grains, and the grain growth path goes through the pure Ni interlayer to consume the higher strain energy [50,51]. This is one aspect that leads to the formation of abnormally large grains in the bonding regions of the original joint, as shown in Figure 2a,b.

On the other aspect, there is no obstacle to the grain boundary migration due to the absence of γ' in the BM, as shown in Figure 5a,b. On the third aspect, the application of Ni interlayer in the welding process promotes atom diffusion [12,52], which accelerates the grain boundaries mobility and grain coalescence. It can be deduced that the formation of abnormal grains in the bonding region is the result of integrating the above three effects, leading to the grain size increase largely from 20.06 μm on average to 60.12 μm .

Apart from the abnormally large grain size, a notable characterization, i.e., most of the large grains with a near $\langle 111 \rangle$ preferred orientation in the X direction (the external stress direction or the normal direction to the bonding interface) and less with a near $\langle 001 \rangle$ orientation, while none with a $\langle 101 \rangle$ orientation was displayed in the bonding region of the original joint, as presented in Figure 2a,b,e,f. Many studies [53,54] illustrated that

the abnormal grain growth was accompanied by the formation of a preferred orientation texture, typically a low-energy, high-symmetry plane. According to the theory, the {111} planes, the close-packed planes of atoms with the lowest surface energy in FCC, satisfy the condition to be the favored orientation, which is consistent with our results for the larger grains in the bonding regions, i.e., the {111} // bonding interface. It can be speculated that the large grains, with the orientation near the {111} // bonding interface, grow much faster than the surrounding grains with other orientations, and even consume other grains by grain boundary migration during the bonding process; as a result, the preferred orientation is produced at last. A similar phenomenon was observed in the in situ annealing process for pure Ni and Cu [51]. In the study, the grains with a special orientation had the priority to grow and consumed the surrounding grains with other orientations, leading to the formation of orientation texture at the stage of abnormal grain growth, where the area fraction of {111} grains rose steeply even from 0%, {001} grain increased during the initial stage, then decreased at the final one, while the {101} grain decreased all the way.

Other studies [55] demonstrated the favored {100}-orientated grains in the abnormal grain growth in FCC films formed after annealing, attributed to the minimization of the strain energy since the <100>-orientated grains have the lowest and equal plane stress (σ_1 and σ_2) and the lowest strain energy density. Alejandro Barrios [56] also revealed that the abnormal grain growth occurred predominantly in the family of grains with <100> orientation along the loading direction during high-cycle loading at room temperature in ultra-fine grained Ni, due to the lowest strain energy density of <100> orientated grains, since the grain elastic anisotropy dictated the thermodynamic driving force of abnormal grain growth at room temperature. In the present work, the study object is a Ni-based alloy block instead of pure Ni film and experiences low static stress and high solid solution temperature, where the capillary effects of GB energy and surface energy play a dominant role in driving grain growth [56]. As a result, in order to balance the surface energy and elastic strain energy, the most abnormal grains with preferred orientation {111} // bonding surface, and fewer with {001} // bonding surface, are formed in the bonding region.

It is reported that oversized grains are not conducive to the TBs formation inside due to the extremely high energy required to introduce multiscale twin architecture [38]. Additionally, the TBs in the grains with small grain sizes or unfavored orientations are consumed, as these grains are swallowed during the abnormal grain growth [57,58], which is the main factor that decreases the TBs density. Eventually, the TBs exhibited extremely fewer number fractions (only 1.98%) in the newly formed large grains of the original joint, compared with that (as high as 50.32%) of the BMs (see Figure 2j).

When the bonding process was modified, the hot forging alloy acted as the initial material before being bonded. The large primary γ' and smaller secondary ones in the BM can provide a pinning force for the grain boundary migration [48,59,60]. Although the γ' can solubilize at the supersolvus temperature (1140 °C for 1 h) in the bonding process, the solution at this condition is a time-consuming process, and the primary γ' perhaps can partly remain, since the solution treatment of FGH96 was carried out at 1150 °C for 2 h in general operation. Hence, the γ' in the material can prohibit effectively the abnormal grain growth during the bonding process.

Identifying the EBSD patterns of the initial material with a hot forging state, the average grain size was about 4.55 μm (Figure 5i), which was much smaller than that both in the matrix region (24 μm) and in the bonding regions (28 μm) of the modified joint, as presented in Figure 2i, indicating that the grains in both the bonding and matrix regions grew during the bonding process. The remaining deformed grains in the BM provide strain energy to support the pre-existing recrystallized grains (with a small GOS value $< 2^\circ$) to grow or to support the deformed grains to continue recrystallization in the whole volume of the material, not restricted within the regions surrounding the pure Ni interlayer during the bonding process. Finally, the deformed grains are consumed to reduce the overall free energy present in the system [61]. As a result, the grains in the matrix region of the modified joint grew from 4.55 μm to 24.06 μm . As to the grains in the bonding region, the

driven force for the grain growth comes from not only the prior deformed grains but also the strain energy in the pure Ni interlayer, leading to relatively larger grains with 28.44 μm . No abnormal grain growth was found in the bonding region, which is different from the case in the original bonding process, as presented in Figure 2c,i, mainly due to the retarding effect of the primary and secondary γ' on the grain boundaries migration, and partly due to the strain energy from the deformed grains, which drive the overall grain growth in the material instead of being limited in the local region surrounding the pure Ni interlayer. Since no abnormal grain formed in the bonding regions and obtained a similar grain size to that of the matrix region, no preferred grain orientation appeared. Furthermore, the number fractions of TBs in both regions are similar.

It can be concluded that abnormal grain growth is the essential prerequisite for the preferred grain orientation formation and decreased TBs. The abnormal large grains, preferred grain orientation, and the TB amount in the bonding regions have a critical role in the mechanical properties of the bonding joint, which will be discussed in Section 4.2.

4.2. The Influence of Abnormal Grains on the Mechanical Properties

The original joint with abnormally large and preferred orientated grains showed weak yield and tensile strengths, as well as high elongation compared with that of the modified joint, as shown in Figure 4. In addition, the fracture types were different, that is, intergranular fracture or intragranular fracture. All the phenomena are related to the different microstructures of joints, hence, the mechanisms of mechanical properties are clarified and checked out below, in aspects of the discrepancy in microstructural characters, including grain size, preferred orientation, and TBs amounts.

Grain refinement is considered an effective hardening route to significantly improve strength based on the Hall–Petch relationship [62], where the yield stress, σ_y , is related to the grain size, d , through the equation: $\sigma_y = \sigma_0 + k_y d^{-1/2}$, in which σ_0 is a lattice friction stress, and k_y is a constant of yielding. According to this expression, it is easily comprehensible that the modified joint gave rise to a higher yield strength compared to the original one, since the grain size in the bonding region of the modified joint is almost half of that of the original, as statistically displayed in Figure 2i. Furthermore, the large number fraction (50.82%) of TBs in the bonding region of the modified joint effectively subdivides the grains, in other words, refines the grains further. As for the original joint, most of the newly formed grains in the bonding regions presented a preferred near $\langle 111 \rangle$ -orientation, hence, the number of grains with obviously different grain orientations that need to be coordinated decreased, which reduces the resistance of metal plastic deformation and joint strength. As a result, the modified joint exhibits a yield strength of 1114.26 MPa and relative yield strength of 99.37%. The value is improved by 10% compared with the original joint.

Figure 6 shows the microscopic strain evolution with increased global strain for the original joint calculated by SEM-DIC. It can be seen that the strain value in the bonding region was higher than that in the neighboring matrix regions and the discrepancy became increasingly larger with the global strain proceeding, as shown in Figure 6c, indicating that the strain was more and more accumulated in the newly formed large grains and led to fracture at this region, as shown in Figure 4(c4). In detailed observation, the strain was revealed to be mainly concentrated along with the slip bands and intermitted by the HAGBs, suggesting that the abnormal grains are favorable for slip activation and no obstacles for slips exist in the interior of the grain, as presented in Figure 6a,b,d.

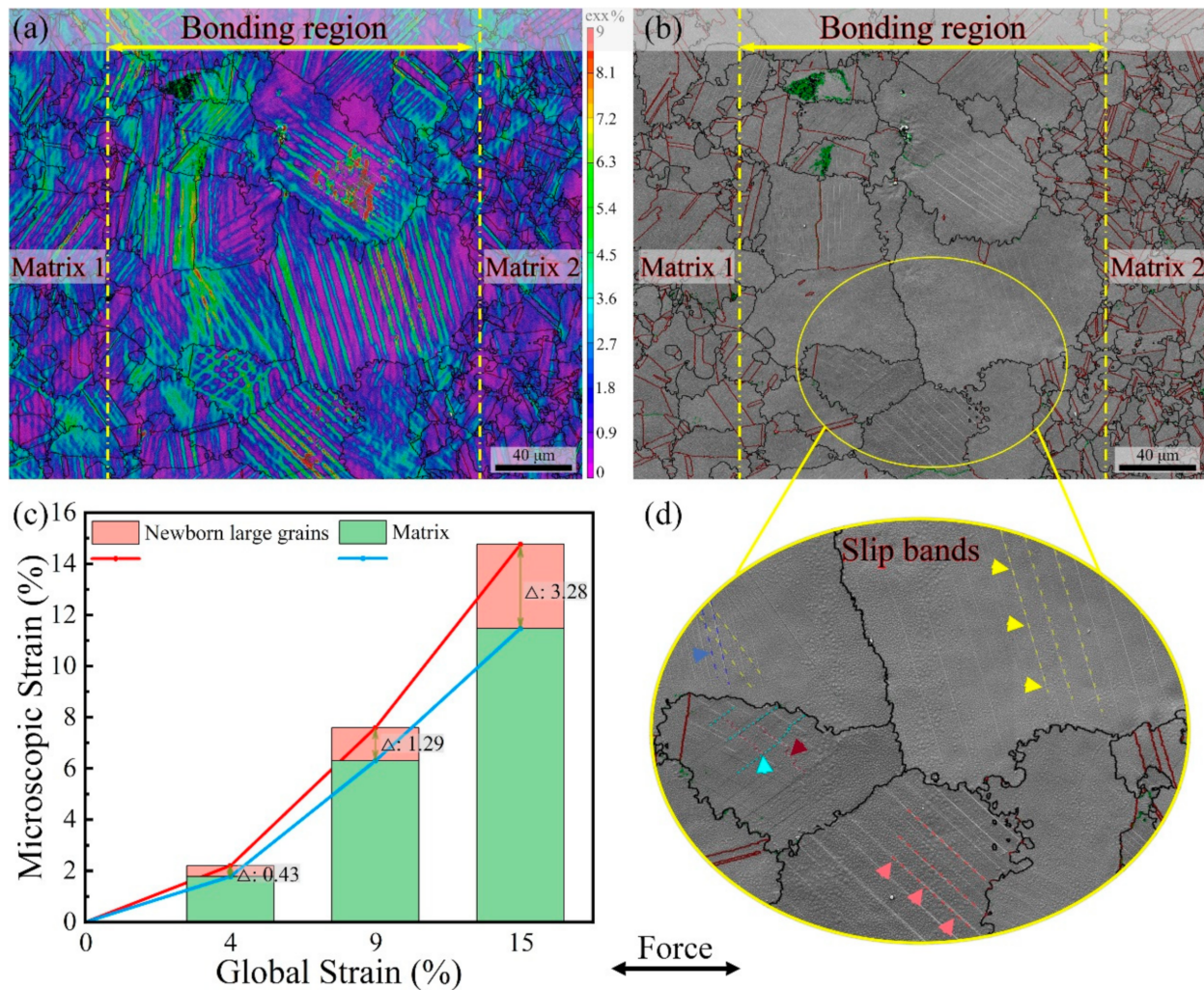


Figure 6. The microscopic strain distribution at 4% global strain by SEM-DIC (a), and the SEM images (b) with a higher magnification (d). The microscopic strain discrepancy between the bonding region and the neighboring matrix region with increased global strain (c).

The tensile strength or strain-hardening ability and the ductility are strongly controlled by the blocking of dislocation motion and the number of activated slip systems in the deformed process. According to Kocks [63], work hardening is a consequence of the fact that some fraction of mobile dislocations are stored in the crystals or react with other dislocations to form new obstacles (obstacle dislocations) and then impede the continued slips, which is linked to the change in obstacle dislocation density during plastic deformation, i.e., $d\rho = d\rho_{\text{STOR}} - d\rho_{\text{RECOV}}$, where $d\rho_{\text{RECOV}}$ is related to the recovery of dislocations already stored, which decreases the work-hardening rate, and $d\rho_{\text{STOR}}$ is related to dislocation storage and enhances the work-hardening rate due to increasing obstacle density. $d\rho_{\text{STOR}}$ is inversely proportional to the mean free path for the mobile dislocation. In the original joint, the abnormal grains provide a larger mean free path for the mobile dislocation, and most of the mobile dislocations exit through the specimen surface without any obstacles in the interior of the grain, and the only obstacle resource is the HAGBs, hence, the obstacle dislocation density is low in the abnormal grains, leading to adverse work-hardening ability. In order to support the speculation, TEM observations for the dislocation at different sites of the bonding region were carried out when the original joint deformed to 20% global strain, as shown in Figures 7 and 8. The specimens were prepared by the focused ion beam (FIB) technique combined with EBSD in order to identify the sites of specimen extraction. Figure 7a showed the dislocation morphology in the interior

of the abnormal grain, displaying that the dislocations lined regularly in the slip bands and escaped from the specimen surface without any obstacles, and no dislocation tangles formed. It can be indicated that rare obstacle dislocations are stored in the interior of abnormal grain and induce work hardening. Turn sight to the HAGB in the bonding region, abundant dislocations were effectively impeded and stacked (in Figure 7c,f,g), suggesting that the work-hardening effect mainly comes from the HAGB for the abnormal grains. The phenomenon of the dislocations proved the Kocks theory in our case. When the bonding process was modified, the smaller grain sizes reduced the mean free path of dislocations, rendering a much higher work-hardening ability. Additionally, a large concentration of TBs present in the microstructure can serve to effectively resist dislocation motion [25,49,64] and give rise to nonuniform plastic microstrain due to the local strain accommodation, so as to raise the resistance ability of the alloy to plastic deformation [38,44]. The blocking interaction between the TB and dislocations was presented in Figure 7d,e, which confirms the contribution of TBs to the strain hardening ability.

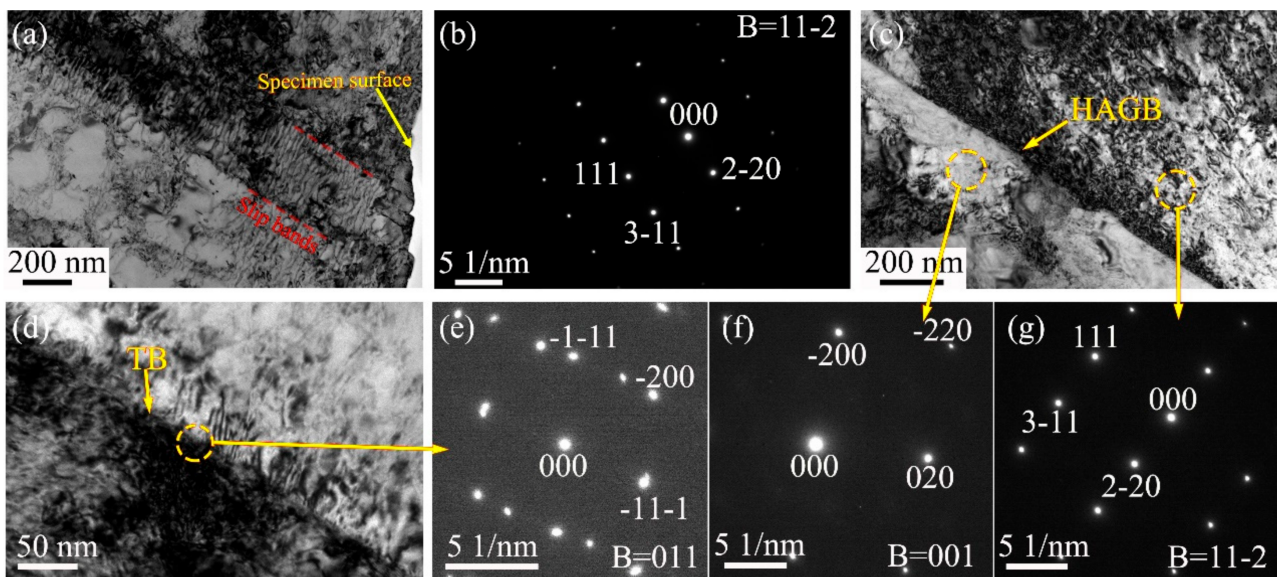


Figure 7. The bright-field images of the dislocation in the abnormal grain interior of the original joint at 20% global strain (a) and the corresponding selected area electron diffraction (SAED) of the matrix via $B = 11-2$ (b). The dislocation morphology at the HAGB (c), the twin boundary (d), and corresponding SAED patterns (e–g).

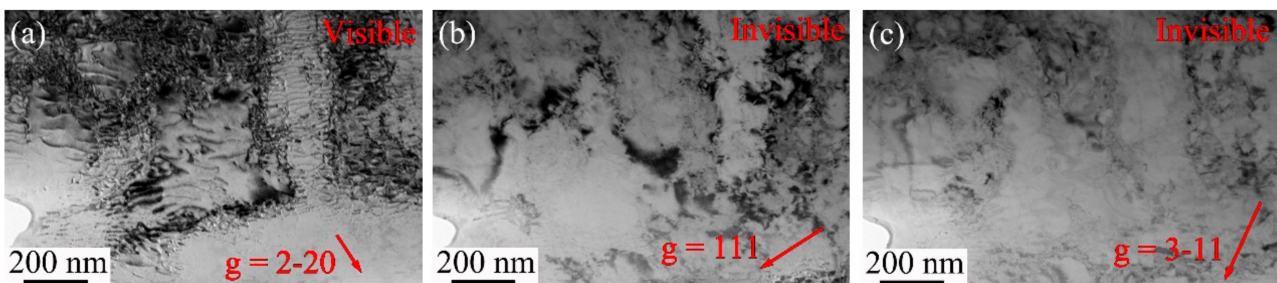


Figure 8. The bright-field images of dislocation under two-beam diffraction conditions for Figure 7a: (a) $g = 2-20$, (b) $g = 111$, and (c) $g = 3-11$.

The preferred orientated morphologies usually lead to anisotropic strengthening and deformation behaviors [31,65]. In order to clarify the relationship between the preferred grain orientation and microscopic deformation evolution, quasi in situ tensile tests combined with EBSD analyses for the same region were carried out on the original joint with

incremental degrees of global strains, and the obtained results are shown in Figure 9. Several abnormal grains (G1U–G5D) in the bonding region were taken into analysis. According to the two-beam electron diffraction analysis and the judge criterion of the dislocation burger vector, i.e., $\vec{g} \cdot \vec{b} = 0$, $\{1-11\} \langle -112 \rangle$ dislocations were identified to be activated, as presented in Figure 8, and then the Schmid factors (SF) evolution for this kind of dislocation are shown in Figure 9b. It can be seen that the SFs of the abnormal grains were lower than those of smaller grains in the surrounding matrix regions and became lower all the way with the increasing global strain and orientation rotations, as presented in Table 2, indicating that the abnormal grains with preferred near $\langle 111 \rangle$ -orientations were not favorable for slip activation and movements, that is, the $\langle 111 \rangle$ -orientated grains should have more plastic strain resistance and lead to higher alloy strength, however, it is inconsistent with the experimental results shown in Figure 6. Consequently, it can be inferred that the softening effects coming from the abnormal grain size and the absence of TBs surpass the hardening effect of orientation. In conclusion, the strengths of the bonding joint are not determined by a single factor, but by a comprehensive consideration. Finally, the modified joint triggered a higher tensile strength (1565.83 MPa) than that of the original one (1465.67 MPa).

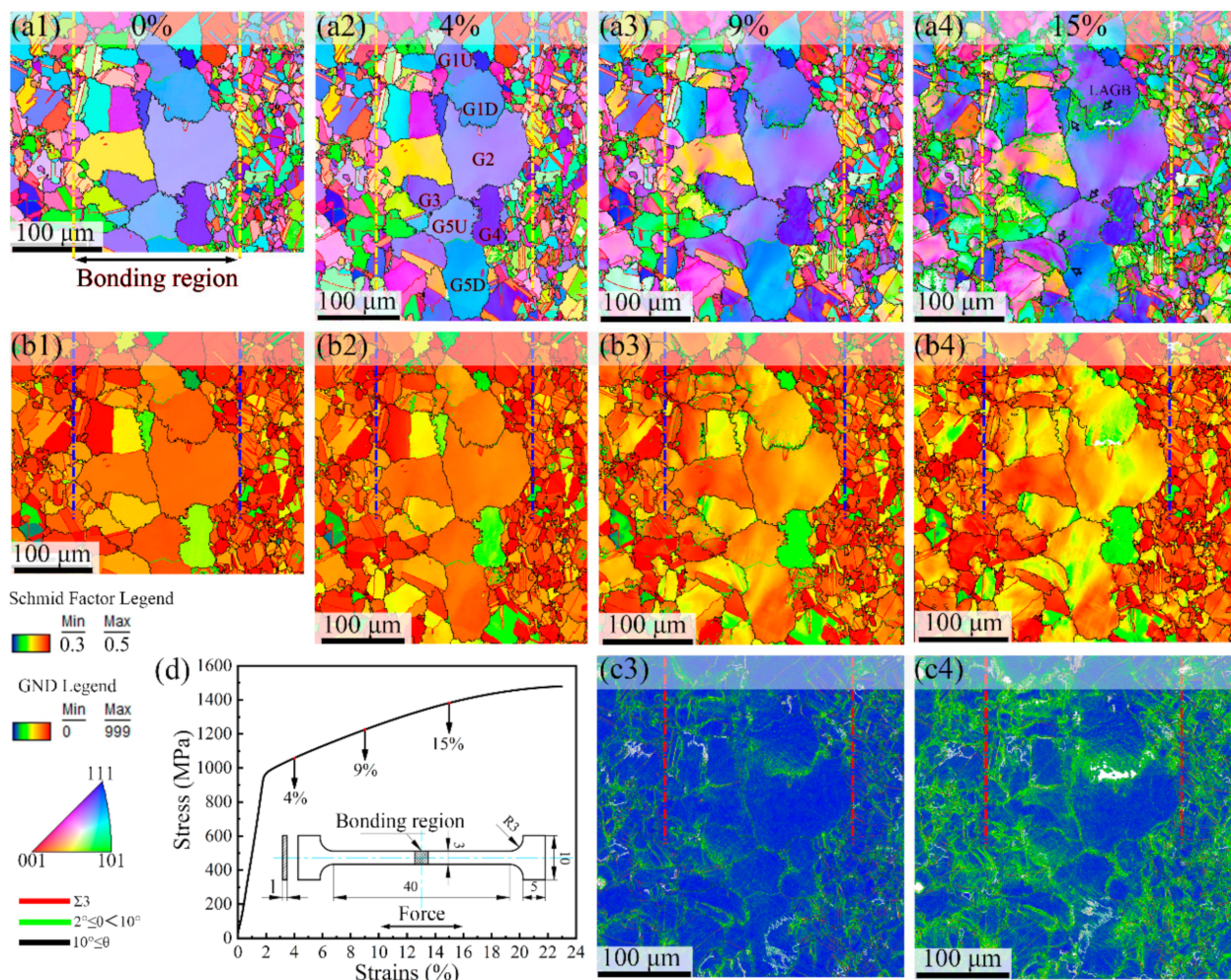


Figure 9. The EBSD patterns evolution of the original joint at different global strains. Orientation image microscopy maps (OIMs) with corresponding inverse polar figure (IPF)//X-axis (the stress direction) (a1–a4), Schmid Factor for $\{111\} \langle -112 \rangle$ slips systems (b1–b4), and GND (c3,c4), (d) the preset engineering strain values for quasi in situ EBSD observation, and the dimensions of the tensile specimen with the stress direction (the inserted figure).

Table 2. The Schmid factors for several abnormal grains in Figure 8 at different global strains.

Global Strain		0%	4%	9%	15%
Grain	Slip System	{111}	{111}	{111}	{111}
		<11-2>	<11-2>	<11-2>	<11-2>
	G1U	0.45	0.44	0.41~0.45	0.38~0.45
	G1D	0.46	0.45	0.41~0.44	0.38~0.42
	G2	0.46	0.45	0.42~0.46	0.39~0.45
	G3	0.42	0.42	0.38~0.44	0.36~0.44
	G4	0.39	0.38	0.36~0.38	0.34~0.38
	G5U	0.47	0.46	0.43~0.45	0.39~0.44
	G5D	0.47	0.46	0.42~0.46	0.38~0.47

Traditionally, the strength and ductility of alloy often exhibit the opposite behavior, i.e., higher tensile strength with lower ductility or lower tensile strength with higher ductility, which is known as a strength–ductility trade-off [66]. In our case, the bonding joints also obeyed this rule. The original joint with lower strength exhibited a higher elongation and a relative one (116%) because the abundant dislocations can be easily activated and move in the abnormal grains without obstacles, leading to more plastic deformation, while the modified joint with higher strengths showed a lower elongation due to the fact that the much more microscopic plastic strain needed to be accommodated, resulting from the orientation diversity of fine grains with TBs [44]. It is notable that TBs as a low-energy boundary can improve the tensile strength without sacrificing ductility attributed to their coherent nature [36,67], which can block or transmit incoming dislocations, depending on their characterizations, thus providing strength and ductility, respectively [37]. As a result, although the elongation of the modified joint decreased compared with the original one, the relative elongation still reached 95.25%.

Different fracture types, i.e., intergranular or intragranular types, were found in the original and modified joint. It is suggested that the formation of intergranular cracks (IGCs) strongly depends on the interaction of slip bands with HAGBs, i.e., the piling up of dislocation at the HAGBs, and strain incompatibilities caused by a Schmid or Taylor factor mismatch between neighboring grains [68]. When dislocation carried by the slip bands cannot transfer through a HAGB, localized grain boundary sliding occurs and results in intergranular cracking [69]. For the original joint, the HAGBs in the bonding region are the only obstacle to the slips resulting from the absence of TBs, as revealed in Figure 6. Furthermore, the neighboring grains have similar orientations and Schmid factors, leading to the slips not being able to transmit and abundant dislocations piling up at the HAGB, as shown in Figure 7c. Finally, the lattice curvature and stress concentration are attained at HAGB with increasing global strain, and then the grain boundary crack is promoted and propagated due to the deformation incompatibility between adjacent grains [22,70]. The geometric necessary dislocations (GNDs) evolution with increased global strain, shown in Figure 9c, manifested that the GNDs mainly accumulated at the HAGB, while the GND density in the interior of the abnormal grain was kept lower all the way, demonstrating that the lattice curvature or the change in geometric shape mainly developed at the HAGB. Moreover, the LAGB mainly formed around the HAGB with increasing global strain, as shown in Figure 9a, and provides additional support.

In addition to the effect of dislocation piling up at the HAGB on the IGCs, it is also found that IGCs are related to the inclination of the grain boundary plane to the tensile axis and Schmid factors of the grains adjacent to these grain boundaries. The preferential formation of IGCs is along grain boundaries perpendicular to the tensile axis and adjacent to grains with low Schmid factors. The IGCs are then driven by the normal stresses acting on the grain boundaries [68,71]. For the abnormal grains of the original joint, a higher fraction of HAGBs are normal to the tensile stress (X direction) due to the grain shape adjustment during the bonding process; furthermore, the abnormal grains exhibited lower SFs due to the preferred near <111> orientation, as displayed in Figure 9. As a result, parts of the IGCs are caused by normal stress exerted on the grain boundaries when the

tensile processes proceed. Figure 10 shows that grain reference (referred to grain average orientation) orientation deviation (GROD) for the selected grains in Figure 9 at 15% global strain. The GRODs in the interior of the grains were smaller than 5° (Figure 10g), suggesting a smaller change in orientations. It is noted that the GROD values at the edges reached the highest for every grain, as presented in Figure 10a–f, indicating that higher local misorientation and local strain incompatibility developed at HAGB, and that these locations act as the source and propagation path for cracks. In conclusion, the original joints exhibit an intergranular fracture type due to the comprehensive effect of grain orientation and size, grain shape, and TBs.

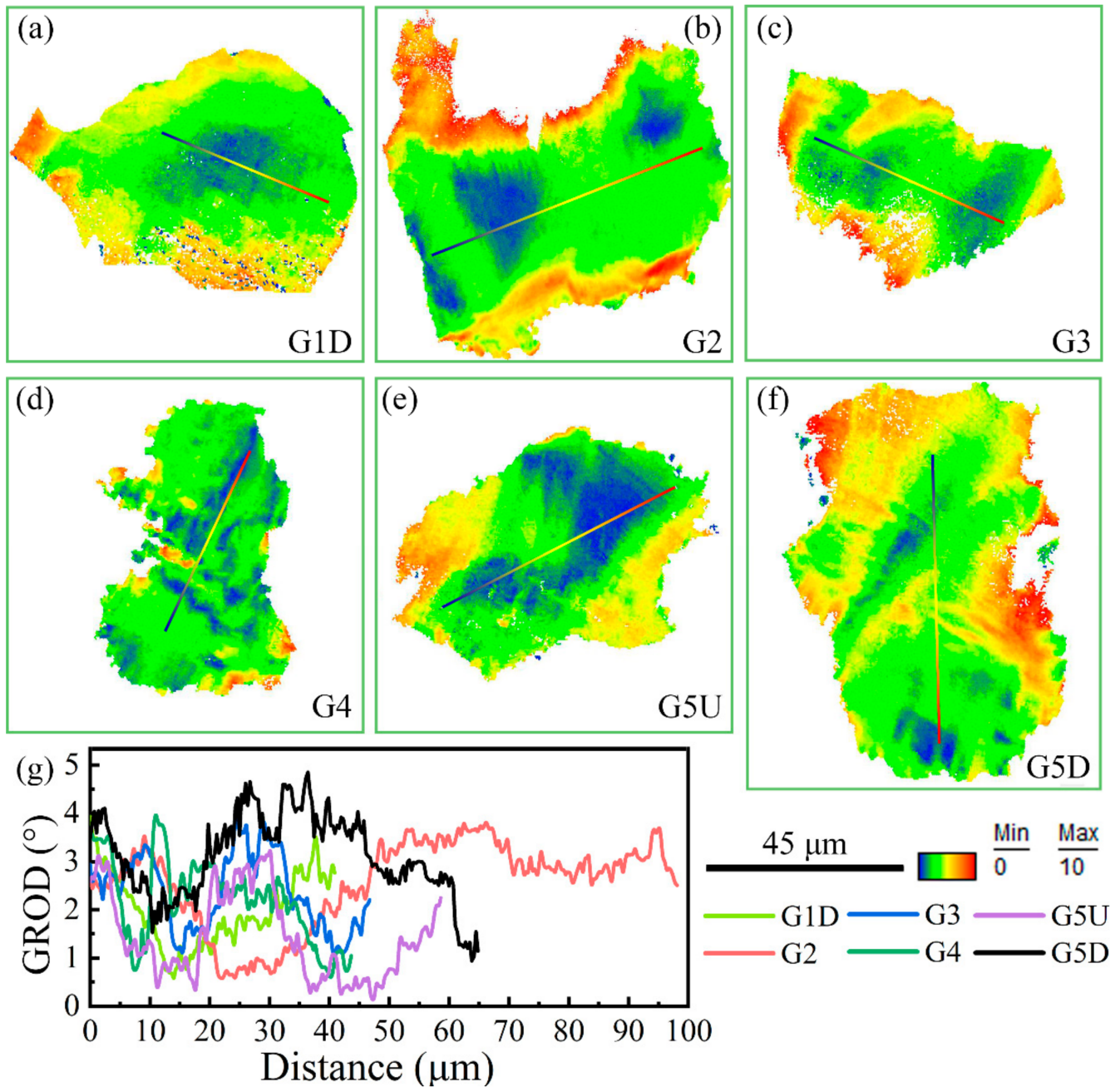


Figure 10. The maps of grain reference (referred to grain average orientation) orientation deviation (GROD) for several grains in Figure 8 at 15% global strain (a–f), and the orientation deviation profile along specific lines in the interior of the grain (g).

After the bonding process was modified, grain orientation diversity and the amount of TBs were introduced to the refined grains in the bonding region. The TBs can either deflect or block crack propagation, which leads to a meandering zigzag propagation path in the interior of the grain [38]. As shown in Figure 4(d2,e2), the twin cleavage planes presented in the fracture surface of BM and the modified joint. More fracture surfaces are created by such a mechanism to dissipate more imposed strain energy, which is helpful to gain better fracture resistance. Due to the strain compatibility between grains with different orientations, and local strain development in the interior of grains under the effect of TBs, new HAGBs are finally formed in the interior of the grains and develop into cracks; finally, the intragranular fracture is developed. This mechanism was detailedly explained and discussed in our previous work [44].

Our present work suggests that tailoring newly formed grain size and introducing twin boundaries, along with eliminating the preferred orientation in the bonding region, can be an efficient way to improve the mechanical properties of the bonding joint. Furthermore, integrating TBs and HAGBs could be promising in the development of strong yet ductile bonding joints.

5. Conclusions

The influence of abnormal grains on the mechanical properties of the FGH96 solid-state diffusion bonding joint was investigated by SEM-DIC combined with EBSD. Based on the obtained results, the major conclusions are as follows:

- (1) The joint characterized by abnormally large grains with preferred orientation in the bonding region has low relative (ratio to the matrix) yield strength (88.81%) and tensile strength (92.54%), but high relative elongation (116.11%). This is attributed to the easier activated slip systems in the large grains and the absent resistance from the twin boundaries.
- (2) The micro-strain, which accumulates at slip bands, escalates in the bonding region with larger grains (2.5 times that of the matrix), leading to failure located at the bonding region. Due to the marginal amount of twin boundaries in this region, the slip systems are mainly retarded by the high-angle grain boundaries, where concentrated stress and lattice curvature would occur, leading to the intergranular fracture.
- (3) After modifying the welding process, the grains in the bonding region are tailored to be close to that of the matrix, along with twin boundaries forming inside. The tensile and yield strength are increased by 100 MPa and 118 MPa, respectively, and the relative tensile and yield strength reach 98.86% and 99.37%, which results from the effect of fine-grained strengthening and twin boundaries on the micro-strain distribution. Furthermore, the fracture mode changes to the intragranular type.
- (4) Tailoring the newborn grain size in the bonding region along with introducing twin boundaries into the grain is an efficient way to improve the mechanical properties of the bonding joint.

Author Contributions: J.Z. formal analysis, software, data curation, investigation, writing—original draft, writing—review and editing; Y.S. methodology, project administration, writing—review and editing, validation; Q.L. methodology, investigation; J.W. methodology, investigation; Y.P. investigation, formal analysis, supervision; S.L. investigation, formal analysis, supervision; S.G. methodology, formal analysis, supervision, funding acquisition, conceptualization, validation. All authors have read and agreed to the published version of the manuscript.

Funding: This research was funded by the National Science and Technology Major Project, China (2017-VI-0016-0088).

Institutional Review Board Statement: Not applicable.

Informed Consent Statement: Not applicable.

Data Availability Statement: Not applicable.

Conflicts of Interest: The authors declare that they have no known competing financial interest or personal relationship that could have appeared to influence the work reported in this paper.

References

1. Peng, Z.; Zou, J.; Wang, X. Microstructural characterization of dislocation movement during creep in powder metallurgy FGH96 superalloy. *Mater. Today Commun.* **2020**, *25*, 101361. [[CrossRef](#)]
2. Zhang, C.; Zhang, L.; Li, M.; Shen, W.; Gu, S. Effects of microstructure and γ' distribution on the hot deformation behavior for a powder metallurgy superalloy FGH96. *J. Mater. Res.* **2014**, *29*, 2799–2808. [[CrossRef](#)]
3. Qiao, S.; Wang, Y.; Lv, L.; Huang, Z.; Tan, G. Normal and abnormal grain growth in a FGH96 superalloy during thermomechanical treatment. *J. Mater. Res. Technol.* **2021**, *15*, 7033–7049. [[CrossRef](#)]
4. Yuli, G.Y.H.S. Thermo-mechanical fatigue behavior of nickel-base powder metallurgy superalloy FGH96 under tension-tension loading. *Acta Metall. Sin. Eng. Lett.* **2010**, *23*, 147–153.
5. Cairo, R.R.; Sargent, K.A. Twin Web Disk-A Step Beyond Convention. *J. Eng. Gas. Turb. Power* **2002**, *124*, 298–302. [[CrossRef](#)]
6. Li, L.; Tang, Z.; Li, H.; Gao, W.; Yue, Z.; Xie, G. Convective heat transfer characteristics of twin-web turbine disk with pin fins in the inner cavity. *Int. J. Therm. Sci.* **2020**, *152*, 106303. [[CrossRef](#)]
7. Zhang, M.; Yao, Q.; Sun, S.; Li, L.; Hou, X. An efficient strategy for reliability-based multidisciplinary design optimization of twin-web disk with non-probabilistic model. *Appl. Math. Model.* **2020**, *82*, 546–572. [[CrossRef](#)]
8. Pouranvari, M.; Ekrami, A.; Kokabi, A. Microstructure evolution mechanism during post-bond heat treatment of transient liquid phase bonded wrought IN718 superalloy: An approach to fabricate boride-free joints. *J. Alloys Compd.* **2017**, *723*, 84–91. [[CrossRef](#)]
9. Arhami, F.; Mirsalehi, S.E.; Sadeghian, A.; Johar, M.H. The joint properties of a high-chromium Ni-based superalloy made by diffusion brazing: Microstructural evolution, corrosion resistance and mechanical behavior. *J. Manuf. Process.* **2019**, *37*, 203–211. [[CrossRef](#)]
10. Xue, H.; Li, T.; Guo, W.; Chen, C.; Zhao, J.; Ding, Z. Effect of graphite content on microstructure and properties of Al_2O_3 ceramic and 304 stainless steel brazed joints. *Mater. Lett.* **2022**, *307*, 131050. [[CrossRef](#)]
11. Xiong, J.; Yuan, L.; Zhu, Y.; Zhang, H.; Li, J. Diffusion bonding of nickel-based superalloy GH4099 with pure nickel interlayer. *J. Mater. Sci.* **2019**, *54*, 6552–6564. [[CrossRef](#)]
12. Zhong, Y.; Xie, J.; Chen, Y.; Yin, L.; He, P.; Lu, W. Microstructure and mechanical properties of micro laser welding NiTiNb/Ti6Al4V dissimilar alloys lap joints with nickel interlayer. *Mater. Lett.* **2022**, *306*, 130896. [[CrossRef](#)]
13. Xu, X.; Ma, X.; Zhao, G.; Chen, X.; Wang, Y. Abnormal grain growth of 2196 Al-Cu-Li alloy weld seams during extrusion and heat treatment. *J. Alloys Compd.* **2021**, *867*, 159043. [[CrossRef](#)]
14. Wei, H.; Tang, J.; Xu, D. Effect of abnormal grain growth on thermoelectric properties of hot-pressed $\text{Bi}_0.5\text{Sb}_{1.5}\text{Te}_3$ alloys. *J. Alloys Compd.* **2020**, *817*, 153284. [[CrossRef](#)]
15. Baure, G.; Zhou, H.; Chung, C.-C.; Stozhkova, M.A.; Jones, J.L.; Nino, J.C. Grain orientation effects on the ionic conductivity of neodymia doped ceria thin films. *Acta Mater.* **2017**, *133*, 81–89. [[CrossRef](#)]
16. Zhang, F.; Zheng, L.; Wang, F.; Zhang, H. Grain orientation dependence of ω phase precipitation in ordered body-centered cubic NiTi based alloys. *Intermetallics* **2019**, *108*, 77–80. [[CrossRef](#)]
17. Wang, Y.; Zhang, Y.; Jiang, H. Effect of grain size uniformity and crystallographic orientation on the corrosion behavior of Mg-2Zn-1Al bar. *Mater. Charact.* **2021**, *179*, 111374. [[CrossRef](#)]
18. Jeng, Y.; Tsai, P.; Chiang, S. Effects of grain size and orientation on mechanical and tribological characterizations of nanocrystalline nickel films. *Wear* **2013**, *303*, 262–268. [[CrossRef](#)]
19. Pushkareva, M.; Sket, F.; Segurado, J.; Llorca, J.; Yandouzi, M.; Weck, A. Effect of grain orientation and local strains on void growth and coalescence in titanium. *Mater. Sci. Eng. A* **2019**, *760*, 258–266. [[CrossRef](#)]
20. Zhao, Z.; Wang, Y.; Safaei, B.; Long, H.; Chu, F.; Wei, Y. Orientation effect on intergranular fracture behaviors along symmetrical tilt grain boundaries in bcc iron. *Mater. Today Commun.* **2021**, *29*, 102981. [[CrossRef](#)]
21. Blochwitz, C.; Jacob, S.; Tirschler, W. Grain orientation effects on the growth of short fatigue cracks in austenitic stainless steel. *Mater. Sci. Eng. A* **2008**, *496*, 59–66. [[CrossRef](#)]
22. Masoumi, M.; Tavares, S.S.M.; Pardal, J.M.; Martins, T.R.B.; da Silva, M.J.G.; de Abreu, H.F.G. The role of microstructure and grain orientations on intergranular cracking susceptibility of UNS 17400 martensitic stainless steel. *Eng. Fail. Anal.* **2017**, *79*, 198–207. [[CrossRef](#)]
23. Zhu, Q.; Wang, C.; Qin, H.; Chen, G.; Zhang, P. Effect of the grain size on the microtensile deformation and fracture behaviors of a nickel-based superalloy via EBSD and in-situ synchrotron radiation X-ray tomography. *Mater. Charact.* **2019**, *156*, 109875. [[CrossRef](#)]
24. Liu, M.; Gong, W.; Zheng, R.; Li, J.; Zhang, Z.; Gao, S.; Ma, C.; Tsuji, N. Achieving excellent mechanical properties in type 316 stainless steel by tailoring grain size in homogeneously recovered or recrystallized nanostructures. *Acta Mater.* **2022**, *226*, 117629. [[CrossRef](#)]
25. Yan, F.; Liu, G.; Tao, N.; Lu, K. Strength and ductility of 316L austenitic stainless steel strengthened by nano-scale twin bundles. *Acta Mater.* **2012**, *60*, 1059–1071. [[CrossRef](#)]
26. Wei, K.; Hu, R.; Yin, D.; Xiao, L.; Pang, S.; Cao, Y.; Zhou, H.; Zhao, Y.; Zhu, Y. Grain size effect on tensile properties and slip systems of pure magnesium. *Acta Mater.* **2021**, *206*, 116604. [[CrossRef](#)]
27. Gabb, T.P.; Kantzos, P.T.; Palsa, B.; Telesman, J.; Gayda, J.; Sudbrack, C.K. Fatigue failure modes of the grain size transition zone in a dual microstructure disk, the minerals, metals and materials society. In Proceedings of the 12th International Symposium on Superalloys, Seven Springs, PA, USA, 9–13 September 2012; pp. 63–72.

28. Gabb, T.; Kantzos, P.; Telesman, J.; Gayda, J.; Sudbrack, C.; Palsa, B. Fatigue resistance of the grain size transition zone in a dual microstructure superalloy disk. *Int. J. Fatigue* **2011**, *33*, 414–426. [[CrossRef](#)]
29. Li, Y.; Wang, L.; Zhang, G.; Zhang, J.; Lou, L. Creep anisotropy of a 3rd generation nickel-base single crystal superalloy at 850 °C. *Mater. Sci. Eng. A* **2019**, *760*, 26–36. [[CrossRef](#)]
30. Li, P.; Yao, W.; Jiang, W.; Han, Q.; Huang, J. Orientation-dependent low cycle fatigue performance of nickel-base single crystal superalloy at intermediate temperature range. *Mater. Today Commun.* **2021**, *26*, 101836. [[CrossRef](#)]
31. Wang, G.; Zhang, S.; Tian, S.; Tian, N.; Zhao, G.; Yan, H. Microstructure evolution and deformation mechanism of a [111]-oriented nickel-based single-crystal superalloy during high-temperature creep. *J. Mater. Res. Technol.* **2022**, *16*, 495–504. [[CrossRef](#)]
32. Li, Y.; Wang, L.; Zhang, G.; Zheng, W.; Qi, D.; Du, K.; Zhang, J.; Lou, L. Creep deformation related to γ' phase cutting at high temperature of a [111] oriented nickel-base single crystal superalloy. *Mater. Sci. Eng. A* **2019**, *763*, 138162. [[CrossRef](#)]
33. Gabb, T.P. The Low Cycle Fatigue Deformation Response of a Single-Crystal Superalloy at 650 °C. *Mat. Sci. Eng. A* **1989**, *108*, 189–202. [[CrossRef](#)]
34. Miner, R.V.; Gabb, T.P.; Gayda, J.; Hemker, K.J. Orientation and Temperature Dependence of Some Mechanical Properties of the Single-Crystal Nickel-Base Superalloy Ren6 N4: Part III. Tension-Compression Anisotropy. *Metall. Trans. A* **1986**, *17*, 507–512. [[CrossRef](#)]
35. Zhang, S.; Liu, W.; Wan, J.; Misra, R.D.K.; Wang, Q.; Wang, C. The grain size and orientation dependence of geometrically necessary dislocations in polycrystalline aluminum during monotonic deformation: Relationship to mechanical behavior. *Mater. Sci. Eng. A* **2020**, *775*, 138939. [[CrossRef](#)]
36. Cooper, R.A.; Wang, Y.; Vignolle, B.; Lipscombe, O.J.; Hayden, S.M.; Tanabe, Y.; Adachi, T.; Koike, Y.; Nohara, M.; Takagi, H.; et al. Revealing the Maximum Strength in Nanotwinned Copper. *Science* **2009**, *323*, 603–607. [[CrossRef](#)]
37. Zhang, Z.; Sheng, H.; Wang, Z.; Gludovatz, B.; Zhang, Z.; George, E.; Yu, Q.; Mao, S.X.; Ritchie, R.O. Dislocation mechanisms and 3D twin architectures generate exceptional strength-ductility-toughness combination in CrCoNi medium-entropy alloy. *Nat. Commun.* **2017**, *8*, 14390. [[CrossRef](#)] [[PubMed](#)]
38. Zhao, S.; Zhang, R.; Yu, Q.; Ell, J.; Ritchie, R.O.; Minor, A.M. Cryoforged nanotwinned titanium with ultrahigh strength and ductility. *Science* **2021**, *373*, 1363–1368. [[CrossRef](#)]
39. Li, J.; Zhang, F. A simultaneously improved strength and ductility on medium Mn TRIP steel designed by pre-twinning strategy based on SFE controlling. *Mater. Lett.* **2022**, *316*, 132078. [[CrossRef](#)]
40. Wang, B.; Liu, H.; Zhang, Y.; Zhou, B.; Deng, L.; Wang, C.; Chen, J.; Zhang, Y. Effect of grain size on twinning behavior of pure titanium at room temperature. *Mater. Sci. Eng. A* **2021**, *827*, 142060. [[CrossRef](#)]
41. Ott, R.; Geng, J.; Besser, M.; Kramer, M.; Wang, Y.; Park, E.; LeSar, R.; King, A. Optimization of strength and ductility in nanotwinned ultra-fine grained Ag: Twin density and grain orientations. *Acta Mater.* **2015**, *96*, 378–389. [[CrossRef](#)]
42. Khorrami, M.S.; Saito, N.; Miyashita, Y. Texture and strain-induced abnormal grain growth in cryogenic friction stir processing of severely deformed aluminum alloy. *Mater. Charact.* **2019**, *151*, 378–389. [[CrossRef](#)]
43. Novikov, V. Texture development during grain growth in polycrystals with strong preferred orientation. *Acta Mater.* **1999**, *47*, 1935–1943. [[CrossRef](#)]
44. Zhang, J.; Shang, Y.; Dong, Y.; Pei, Y.; Li, S.; Gong, S. The crack initiation and strengthening mechanism in FGH96 solid-state diffusion bonding joint by quasi-in-situ SEM-DIC and EBSD. *Mater. Today Commun.* **2022**, *31*, 103689. [[CrossRef](#)]
45. Wright, S.I.; Nowell, M.M.; Field, D.P. A Review of Strain Analysis Using Electron Backscatter Diffraction. *Microsc. Microanal.* **2011**, *17*, 316–329. [[CrossRef](#)]
46. Malta, P.O.; Alves, D.S.; Ferreira, A.O.V.; Moutinho, I.D.; Dias, C.A.P.; Santos, D.B. Static Recrystallization Kinetics and Crystallographic Texture of Nb-Stabilized Ferritic Stainless Steel Based on Orientation Imaging Microscopy. *Metall. Mater. Trans. A* **2017**, *48*, 1288–1309. [[CrossRef](#)]
47. Schuessler, B.J.; Field, D.P.; Overman, N.R.; Joshi, V.V. The Effect of Homogenization Heat Treatment on the Texture Evolution in U-10Mo Alloy. *Metall. Mater. Trans. A* **2021**, *52*, 3871–3879. [[CrossRef](#)]
48. Reeve, J.I.; Schuessler, B.J.; Frazier, W.E.; Field, D.P.; Joshi, V.V. The role of second phase particles and grain boundaries on recrystallization: Quasi-in situ experiments and modeling in U-10Mo alloy system. *J. Nucl. Mater.* **2022**, *559*, 153445. [[CrossRef](#)]
49. McCarley, J.; Tin, S. Understanding the effects of recrystallization and strain induced boundary migration on $\Sigma 3$ twin boundary formation in Ni-base superalloys during iterative sub-solvus annealing. *Mater. Sci. Eng. A* **2019**, *740–741*, 427–438. [[CrossRef](#)]
50. Chen, Z.; Liu, F.; Wang, H.; Yang, W.; Yang, G.; Zhou, Y. A thermokinetic description for grain growth in nanocrystalline materials. *Acta Mater.* **2009**, *57*, 1466–1475. [[CrossRef](#)]
51. Brons, J.; Thompson, G. A comparison of grain boundary evolution during grain growth in fcc metals. *Acta Mater.* **2013**, *61*, 3936–3944. [[CrossRef](#)]
52. Gao, Q.; Jiang, X.; Sun, H.; Song, T.; Mo, D.; Li, X. Interfacial reaction and microstructure investigation of 4J36/Ni/Cu/V/TC4 diffusion-bonded joints. *Mater. Lett.* **2021**, *305*, 130809. [[CrossRef](#)]
53. Humphreys, F.J.; Hatherly, M. *Recrystallization and Related Annealing Phenomena*, 2nd ed.; Elsevier: Pergamon, Turkey, 2004. Available online: <https://www.elsevier.com/books/recrystallization-and-related-annealing-phenomena/rollett/978-0-08-044164-1> (accessed on 22 June 2022).
54. Gottstein, B.; Shvindlerman, L.S. *Grain Boundary Migration in Metals: Thermodynamics, Kinetics, Applications*, 2nd ed.; CRC Press: Boca Raton, FL, USA, 2009.

55. Zhang, J.-M.; Zhang, Y.; Xu, K.-W. Dependence of stresses and strain energies on grain orientations in FCC metal films. *J. Cryst. Growth* **2005**, *285*, 427–435. [[CrossRef](#)]
56. Barrios, A.; Zhang, Y.; Maeder, X.; Castelluccio, G.; Pierron, O.; Zhu, T. Abnormal grain growth in ultrafine grained Ni under high-cycle loading. *Scr. Mater.* **2022**, *209*, 114372. [[CrossRef](#)]
57. Jin, Y.; Lin, B.; Bernacki, M.; Rohrer, G.; Rollett, A.; Bozzolo, N. Annealing twin development during recrystallization and grain growth in pure nickel. *Mater. Sci. Eng. A* **2014**, *597*, 295–303. [[CrossRef](#)]
58. Chen, X.-M.; Lin, Y.; Wu, F. EBSD study of grain growth behavior and annealing twin evolution after full recrystallization in a nickel-based superalloy. *J. Alloys Compd.* **2017**, *724*, 198–207. [[CrossRef](#)]
59. Dennis, J.; Bate, P.S.; Humphreys, F.J. Abnormal grain growth in Al–3.5Cu. *Acta Mater.* **2009**, *57*, 4539–4547. [[CrossRef](#)]
60. Sun, Y.; Fujii, H. Effect of abnormal grain growth on microstructure and mechanical properties of friction stir welded SPCC steel plates. *Mater. Sci. Eng. A* **2017**, *694*, 81–92. [[CrossRef](#)]
61. Wang, X.; Guan, D. The evolution of coarse grains and its effects on weakened basal texture during annealing of a cold-rolled magnesium AZ31B alloy. *J. Magnes. Alloy.* **2022**, *10*, 1235–1241. [[CrossRef](#)]
62. Balasubramanian, N.; Langdon, T.G. The Strength–Grain Size Relationship in Ultrafine-Grained Metals. *Metall. Mater. Trans. A* **2016**, *47*, 5827–5838. [[CrossRef](#)]
63. Mock, F. Laws for Work-Hardening and Low-Temperature Creep. *J. Eng. Mater. T ASME* **1976**, *98*, 76–85.
64. Kvashin, N.; Anento, N.; Terentyev, D.; Serra, A. {111} tilt grain boundaries as barriers for slip transfer in bcc Fe. *Comp. Mater. Sci.* **2022**, *203*, 111044. [[CrossRef](#)]
65. Yang, W.-P.; Li, J.-R.; Liu, S.-Z.; Shi, Z.-X.; Zhao, J.-Q.; Wang, X.-G. Orientation dependence of transverse tensile properties of nickel-based third generation single crystal superalloy DD9 from 760 to 1100 °C. *Trans. Nonferrous Met. Soc. China* **2019**, *29*, 558–568. [[CrossRef](#)]
66. Wang, Y.M.; Voisin, T.; McKeown, J.T.; Ye, J.; Calta, N.P.; Li, Z.; Zeng, Z.; Zhang, Y.; Chen, W.; Roehling, T.T.; et al. Additively manufactured hierarchical stainless steels with high strength and ductility. *Nat. Mater.* **2018**, *17*, 63–71. [[CrossRef](#)]
67. Huang, Q.; Yu, D.; Xu, B.; Hu, W.; Ma, Y.; Wang, Y.; Zhao, Z.; Wen, B.; He, J.; Liu, Z.; et al. Nanotwinned diamond with unprecedented hardness and stability. *Nature* **2014**, *510*, 250–253. [[CrossRef](#)]
68. West, E.; Was, G. Strain incompatibilities and their role in intergranular cracking of irradiated 316L stainless steel. *J. Nucl. Mater.* **2013**, *441*, 623–632. [[CrossRef](#)]
69. Zhang, Z.; Wang, Z. Dependence of intergranular fatigue cracking on the interactions of persistent slip bands with grain boundaries. *Acta Mater.* **2003**, *51*, 347–364. [[CrossRef](#)]
70. Jamali, A.; Ma, A.; LLorca, J. Influence of grain size and grain boundary misorientation on the fatigue crack initiation mechanisms of textured AZ31 Mg alloy. *Scr. Mater.* **2022**, *207*, 114304. [[CrossRef](#)]
71. West, E.; Was, G. A model for the normal stress dependence of intergranular cracking of irradiated 316L stainless steel in supercritical water. *J. Nucl. Mater.* **2011**, *408*, 142–152. [[CrossRef](#)]